Ultrasound in Medicine & Biology 49 (2023) 1212–1226

Contents lists available at ScienceDirect

Ultrasound in Medicine & Biology

journal homepage: www.elsevier.com/locate/ultrasmedbio

Original Contribution

Real-Time Intravital Imaging of Acoustic Cluster Therapy–Induced Vascular Effects in the Murine Brain

Melina Mühlenpfordt[a,b,*], Emma Bøe Olsen[a], Spiros Kotopoulis[a], Sverre H. Torp[c,d], Sofie Snipstad[a,e], Catharina de Lange Davies[a], Marieke Olsman[a]

[a] Department of Physics, Norwegian University of Science and Technology, Trondheim, Norway
[b] Exact Therapeutics AS, Oslo, Norway
[c] Department of Clinical and Molecular Medicine, Norwegian University of Science and Technology, Trondheim, Norway
[d] Department of Pathology, St. Olav's Hospital, Trondheim University Hospital Trondheim, Norway
[e] Cancer Clinic, St. Olav's Hospital, Trondheim, Norway

ARTICLE INFO

Keywords:
Therapeutic ultrasound
Sonopermeation
Increased blood–brain barrier permeability
Drug delivery
Ultrasound contrast agent
Acoustic Cluster Therapy

Objective: The blood–brain barrier (BBB) is an obstacle for cerebral drug delivery. Controlled permeabilization of the barrier by external stimuli can facilitate the delivery of drugs to the brain. Acoustic Cluster Therapy (ACT®) is a promising strategy for transiently and locally increasing the permeability of the BBB to macromolecules and nanoparticles. However, the mechanism underlying the induced permeability change and subsequent enhanced accumulation of co-injected molecules requires further elucidation.
Methods: In this study, the behavior of ACT® bubbles in microcapillaries in the murine brain was observed using real-time intravital multiphoton microscopy. For this purpose, cranial windows aligned with a ring transducer centered around an objective were mounted to the skull of mice. Dextrans labeled with 2 MDa fluorescein isothiocyanate (FITC) were injected to delineate the blood vessels and to visualize extravasation.
Discussion: Activated ACT® bubbles were observed to alter the blood flow, inducing transient and local increases in the fluorescence intensity of 2 MDa FITC–dextran and subsequent extravasation in the form of vascular outpouchings. The observations indicate that ACT® induced a transient vascular leakage without causing substantial damage to the vessels in the brain.
Conclusion: The study gave novel insights into the mechanism underlying ACT®-induced enhanced BBB permeability which will be important considering treatment optimization for a safe and efficient clinical translation of ACT®.

Introduction

The blood–brain barrier (BBB) imposes a challenge for the delivery of therapeutics from the cerebral vasculature to the brain parenchyma [1,2]. Formed from specialized brain endothelial cells, supporting cells (pericytes and astrocytes) and various drug efflux transporters [3], the BBB acts as a protective barrier by preventing the passage of large (>400–500 Da) and hydrophilic molecules, the class in which most neurotherapeutics belong. Therefore, treatment options are limited, despite the increased occurrence of brain disorders such as neurodegenerative diseases and brain cancer.

Current treatments to circumvent the BBB include intranasal delivery, hypertonic mannitol infusion, surgical intervention and the use of carrier molecules [4–7]. However, most methods show a low efficiency, and are non-localized or invasive. An emerging non-invasive strategy to increase the permeability of the BBB locally and temporally is transcranial focused ultrasound in conjunction with systemically administered microbubbles. Several successful experiments on low-power ultrasound and microbubble-mediated increase in BBB permeability have been reported in pre-clinical [8–14] and clinical studies [15–17]. Commercial microbubbles, with number-weighted diameters in the range 2–3 μm and volume-weighted diameters in the range 3–9 μm are designed primarily for diagnostic purposes. These microbubbles typically circulate for 2–3 min and are free flowing in the vasculature, thereby exhibiting only limited contact with the endothelial wall, hampering their effectiveness for therapeutic applications [18,19]. Novel therapeutic microbubble platforms for ultrasound-mediated targeted drug delivery such as Acoustic Cluster Therapy (ACT®; EXACT Therapeutics AS, Oslo, Norway) have been developed to address these drawbacks [20,21].

ACT® is a platform consisting of intravenously administered microdroplet–microbubble clusters that are activated by ultrasound at the targeted site. Ultrasound is then used to drive the bubble oscillations, consequently enhancing the delivery of co-administered therapeutic agents. In brief, with the use of higher-frequency ultrasound (≥2.0 MHz), oscillating microbubbles induce vaporization of the attached microdroplet, forming large, activated ACT® bubbles (median diameter = 22 μm), which transiently lodge in a small fraction of the targeted vasculature (activation step). The second ultrasound exposure, at lower

* Corresponding author. Department of Physics, Norwegian University of Science and Technology, Høgskoleringen 5, 7491 Trondheim, Norway.
E-mail address: melina.muhlenpfordt@ntnu.no (M. Mühlenpfordt).

https://doi.org/10.1016/j.ultrasmedbio.2023.01.007
Received 25 September 2022; Revised 18 December 2022; Accepted 9 January 2023

frequency (~500 kHz), induces controlled volume oscillations of the ACT® bubbles, exerting biomechanical forces on the capillary wall and thereby enhancing the local accumulation of the co-injected therapeutic agent at the target site (enhancement step) [22]. ACT® bubbles address the shortcomings of conventional microbubbles [20,21], such as small size and short circulation times. ACT® bubbles have been designed to lodge at the capillary level and as such are guaranteed to be in contact with the capillary lumen and reside for minutes before they dissolve and dislodge, resulting in increased contact with the endothelium compared with conventional microbubbles [23]. Safety studies have determined that the low density of ACT® bubbles (typically fewer than 4 per mm^3 tissue), deposition at the capillary level and not further up the vascular tree and collateral supply from neighboring capillaries prevent unwanted embolization effects [20,21].

Promising pre-clinical results reveal improved delivery and therapeutic efficacy in solid tumors with no adverse effects [22–27]. Currently, the safety and efficacy of ACT® combined with standard-of-care chemotherapy are being evaluated in a first clinical trial (NCT04021277). Brain tissue exposure to ACT® has been reported to achieve a transient increase in BBB permeability and delivery of polymeric micelles without significant damage to the surrounding tissue [28,29]. In those studies, the increase in BBB permeability induced by ACT® was visualized using contrast-enhanced magnetic resonance imaging (MRI) and near-infrared fluorescence imaging. In addition, confocal microscopic analyses were performed to study ACT®-induced accumulation, extravasation and penetration of co-injected polymeric micelles [29].

Real-time observation using intravital microscopy has emerged as a powerful approach to investigate immediate responses associated with microbubble-mediated BBB permeabilization [30–35]. To deepen our understanding of ACT®-induced enhanced BBB permeability, we used multiphoton intravital microscopy to study the real-time vascular response to ACT®. For this purpose, cranial windows aligned with a ring transducer centered around an objective were mounted to the skull of mice. Then, 2 MDa fluorescein isothiocyanate (FITC)–labeled dextrans were injected to delineate the blood vessels and to visualize extravasation. Histological evaluation of brain sections was performed to assess ACT®-induced tissue damage. Furthermore, brains were treated with ACT® using a single-element dual-frequency transducer, and frozen brain sections were stained and imaged by confocal microscopy to assess changes in perfusion and immune response. The study revealed novel knowledge on the mechanism underlying ACT®-induced enhanced BBB permeability *in vivo*, which will be important in considering treatment optimization for a safe and efficient clinical translation of ACT®.

Methods

Animals

Female albino BL6 mice (6–8 wk of age, ~20 g, n = 20) obtained from Janvier Labs, Le Genest-Saint-Isle, France, were housed in groups of five under conditions free of specific pathogens in a controlled environment (20°C–23°C, humidity of 50%–60%) on a 12-h night/day cycle. Cages were individually ventilated and enriched with housing, nesting material and gnaw sticks in addition to free access to food and sterile water. All animal procedures were approved and in accordance with the guidelines established with the Norwegian Food Safety Authority.

ACT dispersion preparation

The ACT® microbubble/microdroplet cluster dispersion was prepared by reconstituting a freeze-dried suspension of microbubbles of perfluorobutane (PFB, 16 μL/vial) with a microdroplet emulsion of perfluoromethylcyclopentane (PFMCP, 6.8 mg/mL), dispersed in 5 mM tris (hydroxymethyl)aminomethane (TRIS) buffer, forming a 2-mL dispersion [20,21]. The microbubbles were stabilized by a monomolecular phospholipid membrane of hydrogenated egg phosphatidylserine (H-EPS) which is negatively charged, embedded in an amorphous sucrose structure. The microdroplets were stabilized by a monomolecular distearoylphosphatidylcholine (DSPC) phospholipid membrane containing 3% (mol/mol) stearyl amine, making the overall surface positively charged. The reconstituted ACT® formulation consists of 47×106 clusters/mL with a median diameter of 5.6 μm [20]. ACT® was kindly provided by EXACT Therapeutics AS (Oslo, Norway).

Fluorescent tracer

To visualize brain vasculature, 50 μL of 2 MDa FITC–dextran (100 mg/mL in saline; Sigma-Aldrich, Oslo, Norway) was administered intravenously prior to the first ACT® treatment. A 30 μL re-boost was given before every following ACT® treatment. The 2 MDa FITC–dextran was used to provide a size comparable to that of the polymeric micelles used in Olsman et al. [29].

Ring transducer and ultrasound beam profile

A custom-built, single-element, ring-shaped piezoelectric ultrasound transducer (10 mm outer diameter, 1.4 mm thickness, 1.2 mm height) glued to a glass coverslip (φ = 13 mm, No. 1 thickness, Thermo Fisher Scientific, Oslo, Norway) for direct attachment to the skull [36] was used for ACT® treatment. A transducer assembly jig was 3-D-printed to facilitate the alignment of the glass coverslip and the ring transducer. The transducer was driven with a signal generator (33500B, Agilent Technologies, La Jolla, CA, USA), and the signal was amplified with a 50 dB power amplifier (2100L, E&I, Rochester, NY, USA).

The center frequency was 0.84 MHz. The ultrasound beam profile was characterized by attaching the individual ring transducers (n = 3) to extracted mouse skulls and by placing them in a water tank. Furthermore, a water droplet was placed inside the ring transducer to calibrate as closely as possible the experimental conditions. A hydrophone (HGL-0200, Onda, Sunnyvale, CA, USA) connected to a pre-amplifier (AG-2010, Onda) and mounted to a motorized 3-D stage (AIMS III, Onda) was positioned approximately 1–2 mm from the center of the transducer. The acoustic signals measured by the hydrophone were sent to an oscilloscope (5244A, PicoScope, Cambridgeshire, UK) and post-processed on a PC (Soniq Software) (Table 1). The focal size of the activation ultrasound and enhancement ultrasound was extracted from the ultrasound beam profile (Fig. S1, online only). At approximately 1–2 mm distance, the focal diameters of the activation ultrasound (0.84 MHz) and enhancement ultrasound (0.5 MHz) were both 1–2 mm.

Cranial window and ring transducer placement

The cranial window procedure including a video is described in detail in Poon et al. [34]. Briefly, prior to experiments, animals were anesthetized in an induction chamber using 2%–3% isoflurane (Baxter, Iowa, USA) in N_2O (0.4 L/min) and O_2 (0.2 L/min). The anesthesia carrier gas was used to ensure survival of the animal. Thereafter the animals were positioned in a stereotaxic frame (Kopf Instruments, Tojunga, CA,

Table 1
Ultrasound settings for ACT® using a cranial ring transducer

Setting	ACT® activation (60 s)	ACT® enhancement (300 s)
Frequency (MHz)	0.84	0.5
Peak negative pressure (MPa)	0.25–0.3	~0.15
Mechanical index	~0.3	~0.2
Number of cycles	8	8
Pulse repetition frequency (kHz)	1	1

ACT®, Acoustic Cluster Therapy.

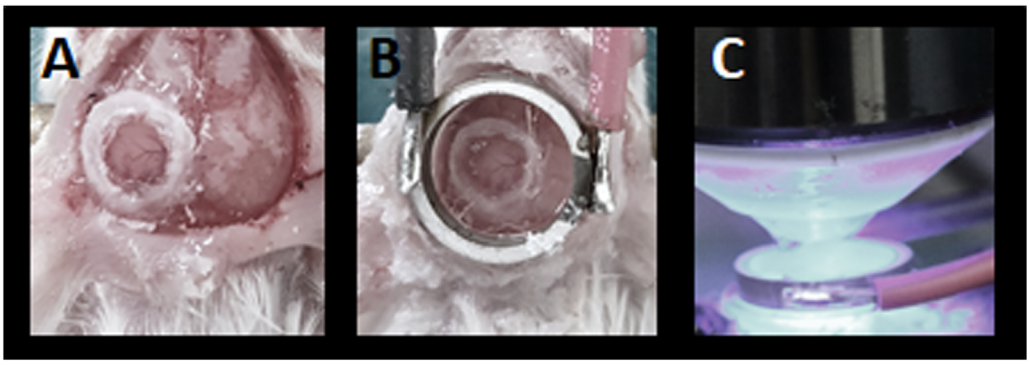

Figure 1. Experimental procedure of intravital multiphoton microscopy imaging. (A) Cranial window situated on the parietal bone sealed with a glass coverslip onto the skull using cyanoacrylate glue. (B) Ring transducer aligned to the cranial window and adhered using 1% (w/v) agarose followed by cyanoacrylate glue. (C) The objective lens of the multiphoton microscope is centered on the ring transducer. FOV, field of view.

USA), and the tail vein was cannulated for easy access to the systemic circulation. During the procedure, the animal's physiology was continuously monitored, and a body temperature of 37°C was maintained using external heating. Before the craniotomy, the fur was removed from the top of the head using a trimmer and depilatory cream (Veet, ON, Canada), and systemic (buprenorphine, 0.05–0.1 mg/kg s.c.), Meloxicam (2–3 mg/kg s.c.) and local (Bupivacaine (1 mg/kg s.c.) analgesia was administered. The scalp was removed using a stereo microscope (10–25×, Nikon, Tokyo, Japan), and a hand drill was used to drill a 3- to 4-mm circular hole into the parietal bone, which was covered with a glass coverslip (φ = 5 mm, No. 1 thickness, Thermo Fisher Scientific) and attached to the skull with superglue (Loctite No. 1363589, Henkel, NRW, Germany) (Fig. 1A). Several droplets of 1% (w/v) agarose were applied on top of the cranial window, and the ring transducer attached to a coverslip was centrally placed on top and glued to the surrounding skull (Fig. 1B). Thereafter, the stereotaxic frame with the animal was transferred to the microscope stage and aligned with the objective lens of the microscope (Fig. 1C).

ACT treatment and imaging procedure

Animals received one to three ACT® treatments, depending on the individual treatment responses, with 10 to 15 min between treatments. One treatment consisted of a bolus injection of 50 µL ACT® clusters prior to 60 s activation ultrasound and 300 s enhancement ultrasound. The ultrasound settings used for the activation and enhancement exposure are given in Table 1.

A timeline of the experimental procedure is illustrated in Figure 2. Animals were injected with 50 µL of 2 MDa FITC–dextran, and a field of view was selected for an XYZ (pre-Z-stack) scan to assess the vasculature prior to ultrasound exposure. Afterward, an XY plane was selected for XYT imaging during ACT® treatment. Animals received one to three ACT® treatments depending on individual treatment responses, with 10 to 15 min between treatments. One treatment consisted of a bolus injection of 50 µL ACT® clusters prior to 60 s activation ultrasound and 300 s enhancement ultrasound. The ultrasound settings used for the activation and enhancement exposure are given in Table 1. Imaging continued throughout the duration of sonication and up to 2 min after treatment. Then, a post-XYZ (post-Z-stack) scan was acquired. Control animals were handled in the same way, either by injecting 50 µL of ACT® without applying ultrasound or by initiating ultrasound without injecting ACT® clusters. The animals were euthanized by cervical dislocation, and the brains were extracted and prepared for histology.

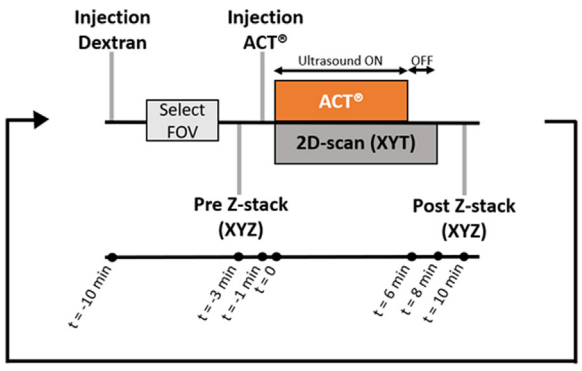

Figure 2. Timeline for the experimental procedure, including injections, ultrasound treatment and post-imaging.

Multiphoton microscope

A multiphoton microscope (*in vivo* SliceScope, Scientifica, Uckfield, UK) with a 20× water dipping objective (XLUMPLFLN 20XW, Olympus, Tokyo, Japan; numerical aperture [NA] = 1, working distance = 2 mm) was used for real-time imaging. The pulsed MaiTai DeepSee (Spectra-Physics, Mountain View, CA, USA) laser was used with an excitation wavelength of 790 nm. The laser power was set to 11%, corresponding to a power of 20 mW as determined by LabMax-TOP Laser Power/Energy Meter (Coherent, Inc., Santa Clara, CA, USA). A 525/50 bandpass filter in front of the GaAsp detector was used to detect FITC–dextran. Images (512 × 512 pixels) were acquired in resonant scanning mode at 31 frames per second (fps) with a field of view of 400 × 400 × 1 µm. During ACT® treatment, an XYT scan was acquired to assess the effect induced by ACT® in real time. Before and after ACT® treatment, an XYZ stack (imaging depth = 100–400 µm, Δz = 1 µm, 12 averages) was acquired to assess the effects induced in three dimensions.

Image analysis

The acquired images and videos were analyzed using Fiji (1.51i, ImageJ, National Institutes of Health, Bethesda, MD, USA) and MATLAB (The MathWorks, Natick, MA, USA). The signal-to-noise ratio of the acquired videos was enhanced by frame averaging (n = 2–4) with Fiji.

Volume determination of red blood cells and ACT® bubbles

All videos acquired were visually assessed for the presence of ACT® bubbles. ACT® bubbles were visualized as non-fluorescent voids (*black*) with a predominantly ellipsoid shape surrounded by FITC–dextran fluorescence. Once observed, the size of the determined ACT® bubble was measured over several consecutive frames (n = 2–7) with the measuring tool in Fiji. The size of the red blood cells (RBCs) was calculated on the basis of profile plots acquired with Fiji and further analysis by a

custom-made MATLAB script (Fig. S2, online only). Volumes of both the ACT® bubbles and RBCs were calculated with the following formula: $(\pi/4) \times (\text{width})^2 \times \text{length}$.

Size determination of vessel outpouchings and corresponding extravasation area and time

Both the length and width of the vessel outpouchings that appeared on the vessel wall were determined with the measuring tool "freehand straight line" in Fiji. For the measurement, the last frame of the video prior to extravasation was used. The size of the corresponding extravasation area was determined with the freehand selection tool in the last frame in which extravasation was still visually observed. The extravasation time was defined as the time between the onset and cessation of extravasation.

Determination of the diameter of blood vessels

In Fiji, a line (approximately 100 μm long) was drawn perpendicular to the blood vessel of interest. For each frame of the video, the intensity profile plot of this line was obtained. These profile plots were processed in MATLAB using a custom-made script to determine the full width at half-maximum (FWHM) of each intensity profile plot.

Measuring fluorescence intensity in blood vessels

To assess if the presence of ACT® bubbles altered the intravascular FITC–dextran fluorescence intensity, three circular regions of interest (ROIs) were placed inside the blood vessels while ACT® bubbles passed through, and the fluorescence intensity was determined in Fiji. One of the ROIs was placed at the location of the transiently stuck ACT® bubble, while the other two ROIs were placed just behind and in front of the ROI. Of all three ROIs, the average intensity per video frame was determined and plotted.

Videos acquired from real-time imaging

A total of 20 animals were used to conduct real-time intravital microscopy experiments. From successful experiments (n = 6–7 animals), approximately 200 videos were acquired during ACT® treatment, and 50–60 videos represent Z-stacks prior to and after ACT® treatment. The results described in this study are based on 30–40 videos, as not all ACT® treatments resulted in measurable effects in the field of view.

Histology

For histological evaluation, excised brains from real-time imaging experiments were cut with a scalpel to a size that included the hemisphere that contained the cranial window and the contralateral hemisphere. Afterward, the brain tissue was fixed in 4% formalin and embedded in paraffin. Brains were serially sectioned every 100 μm transversely from the surface until 2 mm into the brain. The 4-μm-thick sections were stained with hematoxylin, erythrosine and saffron (HES). Tile scans of the HES sections were acquired using bright-field imaging with an LSM800 (Zeiss, Oberkochen, Germany) and a 20×/0.8 Plan-Apochromat air objective. A senior neuropathologist, blinded to the study, assessed the brain sections for tissue damage induced by cranial window placement or ACT® treatment.

Immunohistochemistry

For immunohistochemical analyses, frozen brain sections were stained with the following primary antibodies: anti-CD31, as endothelial marker to assess vascular changes, anti-Claudin 5, for tight junction complexes, anti-F4/80, as a marker for macrophages, anti-TMEM119 as a microglia specific marker and anti-Ly6G for neutrophils to assess potential immune responses (Table 2).

Brain sections were obtained from a separate study [29] in which the entire brain was treated with a dual-frequency transducer [37] and excised 1 or 24 h after ACT® treatment. The reason for analyzing these brain sections in addition was the larger ACT®-exposed areas (−3-dB beamwidth of 6 mm (0.5 MHz) and 16 mm (2.7 MHz)) as well as the two time points. Furthermore, the effect craniotomy had on the brain could be excluded by analyzing these sections. Before euthanization of the animals, FITC-labeled *Lycopersicon esculentum* (tomato) lectin (FITC–lectin, Vector Laboratories, Burlingame, CA, USA) was intravenously injected to stain for functional vessels at that time point.

Briefly, 10- or 25-μm-thick sections from one or two brain depth levels were thawed at room temperature (RT) and rehydrated in PBS (pH 7.4). The sections were fixed in acetone/methanol (v/v) at −20°C for 90 s. Non-specific staining was blocked for 1 h at RT using 0.2% bovine serum albumin (BSA) in PBS supplemented with 0.2 % Triton X-100 for permeabilization. Sections were then incubated for 1 h at RT using the primary antibodies (anti-CD31, anti-Claudin 5, anti-F4/80, anti-TMEM119, anti-Ly6G) in blocking buffer containing 1% BSA in PBS supplemented with 0.3% Triton X-100. Thereafter, the sections were washed 3 × 5 min in PBS.

The following secondary antibodies were used: Alexa Fluor 647 conjugates (AF-647) as well as Cy3 conjugates (Table 2). The secondary antibodies were diluted in a blocking buffer containing 1% BSA and 0.3% Triton X-100, and sections were incubated with the antibodies for

Table 2
Primary and secondary antibodies used for immunohistochemistry

pAB and sAB	Species	Dilution (μg/mL)	Thickness of section (μm)	Manufacturer and product number
pAB: Anti-CD31	Rat anti-mouse	10	25	BD Bioscience (550274)
sAB: Alexa Fluor 647-conjugated	Donkey anti-rat	10		Dianova (712-605-153)
pAB: Anti-Claudin 5	Mouse	1.25	10	Thermo Fisher Scientific (35-2500)
sAB: Alexa Fluor 647-conjugated	Goat anti-mouse	2		Thermo Fisher Scientific (A-21235)
pAB: Anti-F4/80	Rat anti-mouse	20	10	Bio-Rad Laboratories (MCA497G)
sAB: Alexa Fluor 647-conjugated	Donkey anti-rat	7.5		Jackson ImmunoResearch (712-605-153)
pAB: Anti-TMEM 119	Rabbit anti-mouse	1	10	Abcam (ab209064)
sAB: Cy3-conjugated	Anti-rabbit	1.5		Jackson ImmunoResearch (711-166-152)
pAB: Anti-Ly6G	Rabbit anti-mouse	7	10	Abcam (ab238132)
sAB: Cy3-conjugated	Anti-rabbit	1.5		Jackson ImmunoResearch (711-166-152)

pAB, primary antibody; sAB, secondary antibody.

1 h at RT in the dark. Afterward, the sections were washed 3 × 5 min with PBS and mounted with Vectashield Vibrance (Vector Laboratories), with or without 4′,6-diamidino-2-phenylindol (DAPI) nuclear stain depending on the applied staining and covered with a coverglass.

Confocal laser scanning microscopy of brain sections and image analysis

Tile scans

Immunohistochemically labeled brain sections were imaged with an LSM 800 from Zeiss. Tile scans of anti-CD31 stained brains were acquired using a 20×/0.8 plan Apochromat air objective (16 bit, 1024 × 1024 pixels, 312 nm pixel size, two averages by line, 10% overlap between consecutive tiles, optical slice thickness of 10 μm). Brain sections also contained FITC–lectin- and rhodamine B-labeled polymeric micelles, the accumulation of which after ACT® was observed in an earlier study [29]. Tile scans of anti-F4/80- and DAPI-stained sections were acquired using a 20×/0.50 Plan-Neofluar air objective (8-bit, 1024 × 1024, 312 nm pixel size, two averages per line, 10% overlap, optical slice thickness 6 μm). To minimize fluorescent spillover, the different channels of the image were captured in a sequential manner. The fluorophores, their respective excitation and emission wavelength and light sources are depicted in Table 3. The fraction of perfused vessels was calculated from tile scans by dividing the area fraction of FITC+ blood vessels by the area fraction of CD31+ vessels.

High-magnification imaging

Regions of interest within sections were imaged using a 20×/0.8 plan Apochromat air objective or a 40×/1.2 C-Apochromat water objective (For both objectives: 16-bit, 1024 × 1024 pixels, 0.156–0.312 μm/pixel, line average of 4, optical slice thickness 1.9 μm). Each fluorophore was captured in a different channel, and imaging was done sequentially (Table 3).

Temperature measurements

To determine if multiphoton imaging caused a temperature increase and potentially activated ACT® clusters, 50 μL of the ACT® cluster dispersion was deposited on a microscope glass slide (Fig. S3, online only). The temperature rise was measured using the inbuilt temperature measuring capabilities of a fiberoptic needle hydrophone (Precision Acoustics, Dorchester, UK) while imaging with a near-infrared laser (Chamelein Vision-S IR pulsed laser, Olympus, Tokyo, Japan) at a wavelength of 790 nm. The laser power was measured at different power levels using a LabMax-TOP Laser Power/Energy Meter (Coherent, Inc.). XYT scans were collected with a Leica TCS SP (10×/0.40 HC PL Apo CS air objective). To assess if the temperature rise induced by the multiphoton laser could affect ACT® bubble activation (bubbles with diameters ≥20 μm were regarded as "activated"), 15 μL of the ACT® dispersion was deposited on a microscope glass slide. A white light laser was used for bright-field transmitted light imaging. The effect of the 790 nm excitation laser was evaluated at three different power levels (20, 40 and 60 mW). Repeated XY scanning at fixed power was done at 2.4 μs/pixel speed for a total of 10 min, capturing transmitted light images (512 × 512 pixels, 8 bit, 2.27 μm pixel size) every 2 min.

Table 3
Fluorophores and respective excitation and emission wavelengths used for confocal laser scanning microscopy tile scans and high-magnification images using a diode laser as a light source

Fluorophore	Excitation wavelength (nm)	Emission wavelength (nm)
Tile scan settings		
FITC-lectin	488	495–540
AF-647	640	656–700
Rhodamine B	561	570–700
DAPI	405	410–546
High-magnification image settings		
FITC-lectin	488	490–560
AF-647	640	656–700
Rhodamine B	561	570–620
DAPI	405	410–546
Cy3	561	565–630

DAPI, 4′,6-diamidino-2-phenylindol; FITC, fluorescein isothiocyanate.

Statistics

Statistical analyses of the acquired data sets were performed using GraphPad Prism, version 8.0 (GraphPad Software, Boston, MA, USA). The type of statistical test used is indicated in the corresponding figure caption. A p value <0.05 indicates statistical significance.

Results

Activated ACT® bubbles in brain capillaries

During ACT® treatment, anticipated ACT® bubbles appeared as dark spheres or ellipsoids in the fluorescent vasculature. Figure 3 provides snapshots of acquired videos with anticipated ACT® bubbles (Videos S1–S4, online only).

From 64 observations, the average volume of the anticipated ACT® bubbles was 965 ± 1485 μm^3, with the smallest and largest observed ACT® bubbles being 185 μm^3 (corresponding diameter approximately 7 μm) and 9622 μm^3 (corresponding diameter approximately 26 μm), respectively. The red blood cells (n = 5949) had an average size of 144 ± 57 μm^3 and differed significantly from the average volume of the anticipated ACT® bubbles ($p < 0.0001$). The average volumes of both the RBCs and ACT® bubbles are given in Figure 4.

Transient vasomodulation in response to sonication

During ACT® treatment, variation in the diameter of blood vessels in the field of view was observed. In two consecutive treatments of one animal, two vessels responded to the ultrasound (Fig. 5, snapshot from Videos S5 and S6 [online only]). During the first treatment (Fig. 5A), the vessel in the top right (*green line*) started to deform from approximately the moment the ultrasound was turned on. The diameter of the vessel was reduced by 85 % (60–10 μm) before the diameter increased to 40 μm again. Another vessel (*orange line*) had an initial diameter of around 13 μm, which changed by approximately 5 μm (40% reduction) in a pulsed manner several times. The diameters of two other blood vessels (*red and blue lines*, 70 and 5 μm, respectively) in the field of view were measured as well but did not change during ultrasound exposure. During the second treatment (Fig. 5B), which was initiated approximately 9 min after the first treatment, the four blood vessels exhibited behavior similar to that during the first treatment. The *red line* in the graph (Fig. 5Aiii) is noisier compared with the *red line* in Figure 5B because of a difference in contrast between the videos. In addition, some motion artifacts were observed at the start of the video corresponding to Figure 5A. The diameters of the four measured blood vessels during the first and second treatment can be found in Figure 5A and 5Biii. Even though the observations cannot be directly attributed to lodged ACT® bubbles in the field of view, vasomodulation started when the ultrasound was on, indicating that ACT® could be responsible for the observed vasomodulation.

FITC–dextran fluorescence intensity inside blood vessel

To study if ACT® bubbles cause accumulation of FITC–dextrans while the bubbles were moving or temporarily lodged or obstructed the blood vessel, the fluorescence intensity was measured at different locations in the blood vessel in which an ACT® bubble was observed (Fig. 6).

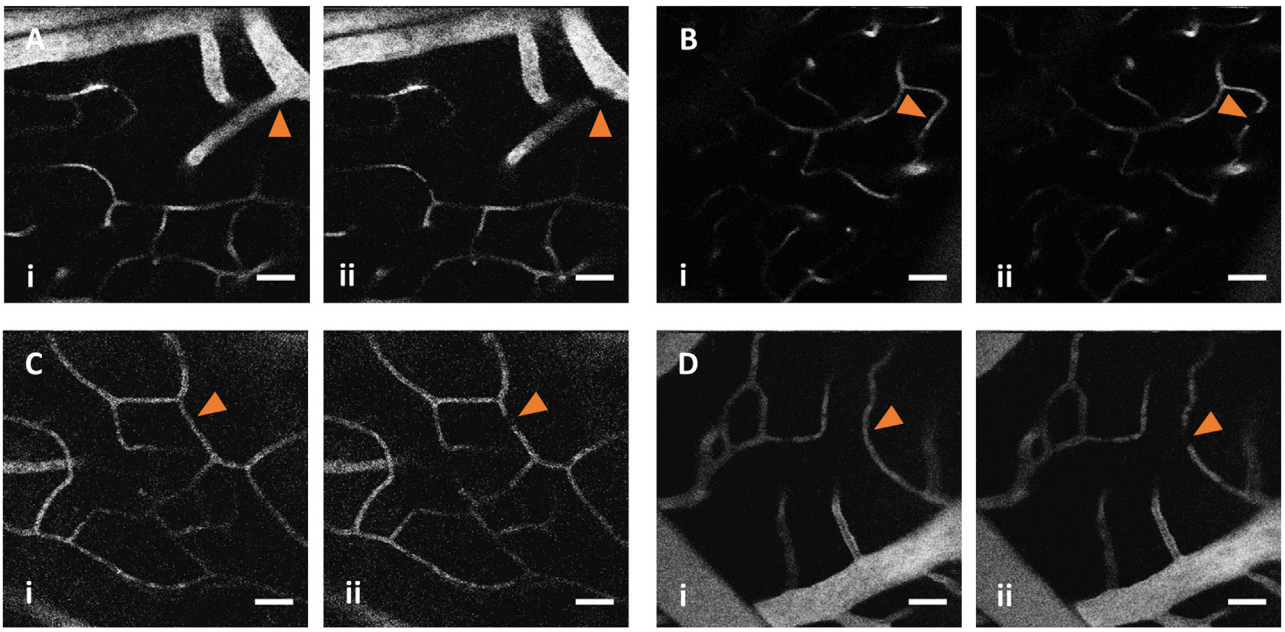

Figure 3. Representative Acoustic Cluster Therapy (ACT®) bubble observations. (A–D) Snapshots of acquired videos (i) without and (ii) with a suspected ACT® bubble, which is indicated by an *orange arrowhead*. Bar = 50 μm.

In (Fig. 6Ai) (Video S7, online only) an ACT® bubble appeared in the vasculature and was temporarily lodged in a blood vessel (Fig. 6Aii), indicated by a drop in fluorescence intensity (Fig. 6Aiii) at the specific location (*blue line*). Blockage resulted in a temporary increase/decrease in the fluorescence intensity in the ROIs located upstream/downstream (*green/red line*) of the lodged ACT® bubble. Figure 6B (Video S8, online only) depicts a similar situation: an ACT® bubble is temporarily lodged (Fig. 6Bii) and the fluorescence intensity at the site drops clearly (Fig. 6Biii, *blue line*). While the ACT® bubble is lodged, the fluorescence intensity in the ROI upstream from the microbubble (*green*) increased slightly while the fluorescence intensity in the ROI downstream from the lodged ACT® bubble (*red*) decreased slightly. In Figure 6B, the ACT® bubble seemed to be lodged for a longer time compared with that in Figure 6A as the change in fluorescence intensity was prolonged. In Figure 6C (Video S9, online only), the situation is different because several ACT® bubbles flow through the same blood vessel and become lodged, resulting in fluctuating decreasing and increasing fluorescence intensities (Fig. 6Ciii).

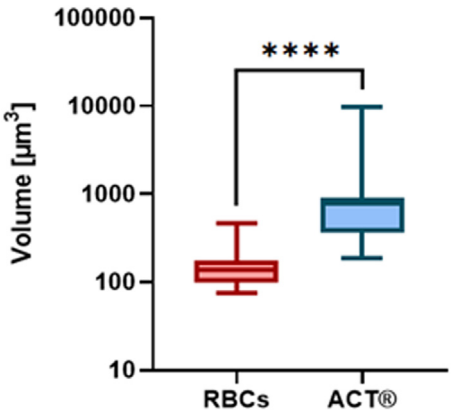

Figure 4. Comparison of volumes of red blood cells (RBCs) and Acoustic Cluster Therapy (ACT®) bubbles. Boxplot reveals the median and standard deviations of the volumes of observed RBCs (n = 5949) and anticipated ACT® bubbles (n = 64). ****$p < 0.0001$.

Extravasation during ACT® treatment

During ultrasound exposure, the growth of eight vessel outpouchings was observed, as indicated by the *orange circles* in Figure 7. The corresponding Videos (S10–S14, online only) illustrate how the small saccular outpouchings develop during ACT®. Eventually, the outpouchings started leaking, and extravasation of FITC–dextrans occurred. No clear extravasation was observed at other locations. The outpouchings in Figure 7H originated on expansion of the outpouching in Figure 7C. The same applies to the outpouching in Figure 7F, which originated from the outpouching shown in Figure 7E. The maximum size of the outpouchings was determined and is given in Table 4. The area of the outpouching prior to leakage varied largely, with the smallest being 43 μm^2 and the largest 100 times larger, 5950 μm^2. The maximum observed penetration depth of 2 MDa FITC–dextrans varied between 10 and 200 μm. Seven of the eight outpouchings leaked while imaging. The corresponding extravasation area and duration were determined (Table 4). No relation between the size of the outpouching prior to leakage and the area of extravasation was found. The duration of the extravasation was independent of the area of extravasation.

Vascular observations post-ACT® treatment

Most information on the mechanism underlying ACT® was obtained by real-time imaging of the murine brain during ACT® treatment. In addition, before and after ACT® treatment, a Z-stack was obtained to compare and assess for ACT®-induced effects at different depths not recorded during real-time imaging. A large fluorescent elliptical structure with a length and diameter of approximately 75 and 50 μm was observed in the post-Z-stack once (Fig. 8ii). After approximately 6 min, the structure had disappeared, leaving a heterogenous fluorescence intensity within the blood vessel (Fig. 8iii). Prior to ACT® treatment, the vasculature in the pre-Z-stack appeared normal (Fig. 8i).

In addition, the vasculature outside the field of view was assessed for ACT®-induced effects post-treatment. Two post-Z-stacks (Fig. S3, online only) resemble the fluorescence intensity pattern observed on formation of the outpouchings during real-time imaging. However, because of the missing pre-Z-stack, the structures cannot be directly attributed to ACT®.

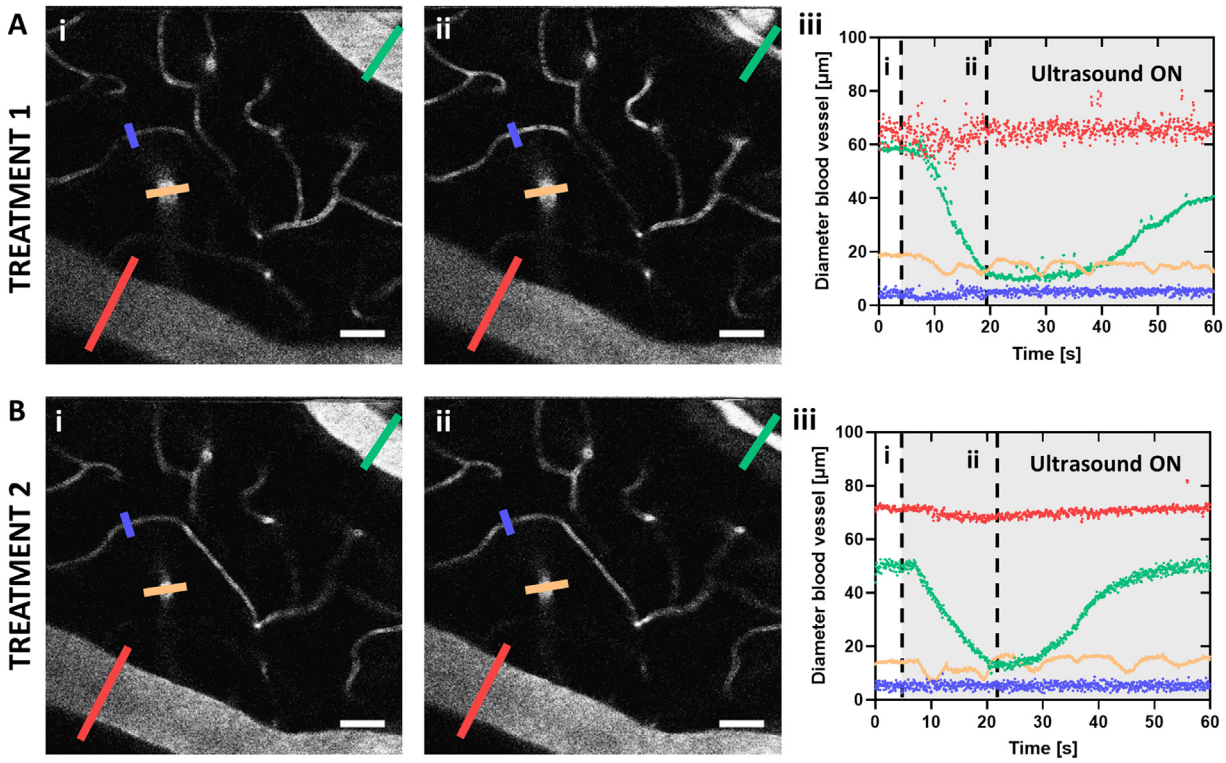

Figure 5. Transient vasomodulation seen as a reduction and extension of the blood vessel diameter in an animal during consecutive (A) first and (B) second Acoustic Cluster Therapy (ACT®) treatments. Per panel, images (i) and (ii) are two snapshots from videos, and the graph (iii) indicates the diameters of the blood vessels of interest over time in the corresponding video. The two *vertical dashed lines* indicate the time points when the snapshots were taken. Bar = 50 µm.

Blood vessels still functional post-leakage of outpouchings

To study whether the vessels where extravasation occurred were still functional, a pre-Z-stack (Fig. 9A) and post-Z-stack (Fig. 9B) of the vasculature were compared. Figure 9B illustrates that the blood vessels in which the outpouching occurred still contained flowing FITC–dextran, indicating that the vessels were still functional (Video S15, online only). The comparison also revealed that several blood vessels were slightly dilated (+1.2–2.1 μm) with respect to their initial size (Fig. 9C) on ACT®. In addition, some blood vessels in the pre-Z-stack were not as clearly visible in the post Z-stack. This might be caused by small misalignments both in the XY-direction and in the Z-direction, because of movement of the blood vessels with respect to each other or change in imaging plane caused by movement of the animal. In addition, the high local concentration of extravasated FITC–dextran will reduce the light penetration depth.

Immunostaining of brain sections after ACT® treatment

To further assess vessel functionality, brains treated in a separate study using a dual-frequency transducer were immunofluorescently labeled and imaged [29]. The advantage of using these brains was that the exposed area was much larger than the exposed area in the cranial window, with −3-dB beamwidths of 6 mm (activation frequency = 2.7 MHz) and 16 mm (enhancement frequency = 0.5 MHz). Furthermore, any effects craniotomy had on the brain could be excluded. Blood vessels were labeled for the endothelial marker CD31 and compared with the FITC–lectin-labeled functional vasculature in control and ACT®-treated brains (Fig. 10). No significant difference in FITC–lectin staining relative to CD31 staining was found for the treated compared with the non-treated brains, neither 1 h nor 24 h after ACT® treatment, indicating that ACT® did not induce any change in perfusion in the brain.

Anti-Claudin 5 staining of tight junctions in brain sections revealed a continuous staining pattern along the endothelial cell lining. In a few cases, vessels had a discontinuous staining pattern with only speckles along the vessel structure in ACT®-treated brains, but also in untreated brains. Visual assessment revealed no difference in the distribution of Claudin 5 in control brains compared with ACT®-treated brains over the entire brain.

Immunolabeled brains also contained fluorescent polymeric micelles, and extravasation sites of these were used to mark areas of increased BBB permeability resulting from ACT® bubble activity. High-resolution images of anti-CD31- and anti-Claudin 5–stained vessels of areas with extravasated polymeric micelles revealed reduced FITC–lectin staining of some vessels in ACT®-treated brains, indicating non-functional vessels during the time of FITC–lectin injection, caused by ACT® bubble activity.

Histological evaluation after ACT® treatment

Microscopic examination of 4 µm HES-stained sections from different depth levels of extracted brains revealed no signs of vascular damage in either the cranial window containing hemisphere or the respective contralateral hemisphere in control and ACT®-treated animals. Figure 11 provides representative tile scans and high-magnification images of the cranial window-containing hemisphere of control and ACT®-treated brains. A small number of vacuoles were detected around the cranial window in the case of one animal. HES sections of ACT®-treated animals showed no acute lesions, no damage or destructed blood vessels compared with control animals. Solely, at a depth of 2 mm, very few RBCs were observed to remain in the blood vessels or be extravasated. Furthermore, there was no increase in polymorphonuclear leukocytes, monocytes or lymphocytes and no detectable assembly of fluid in the sonicated regions.

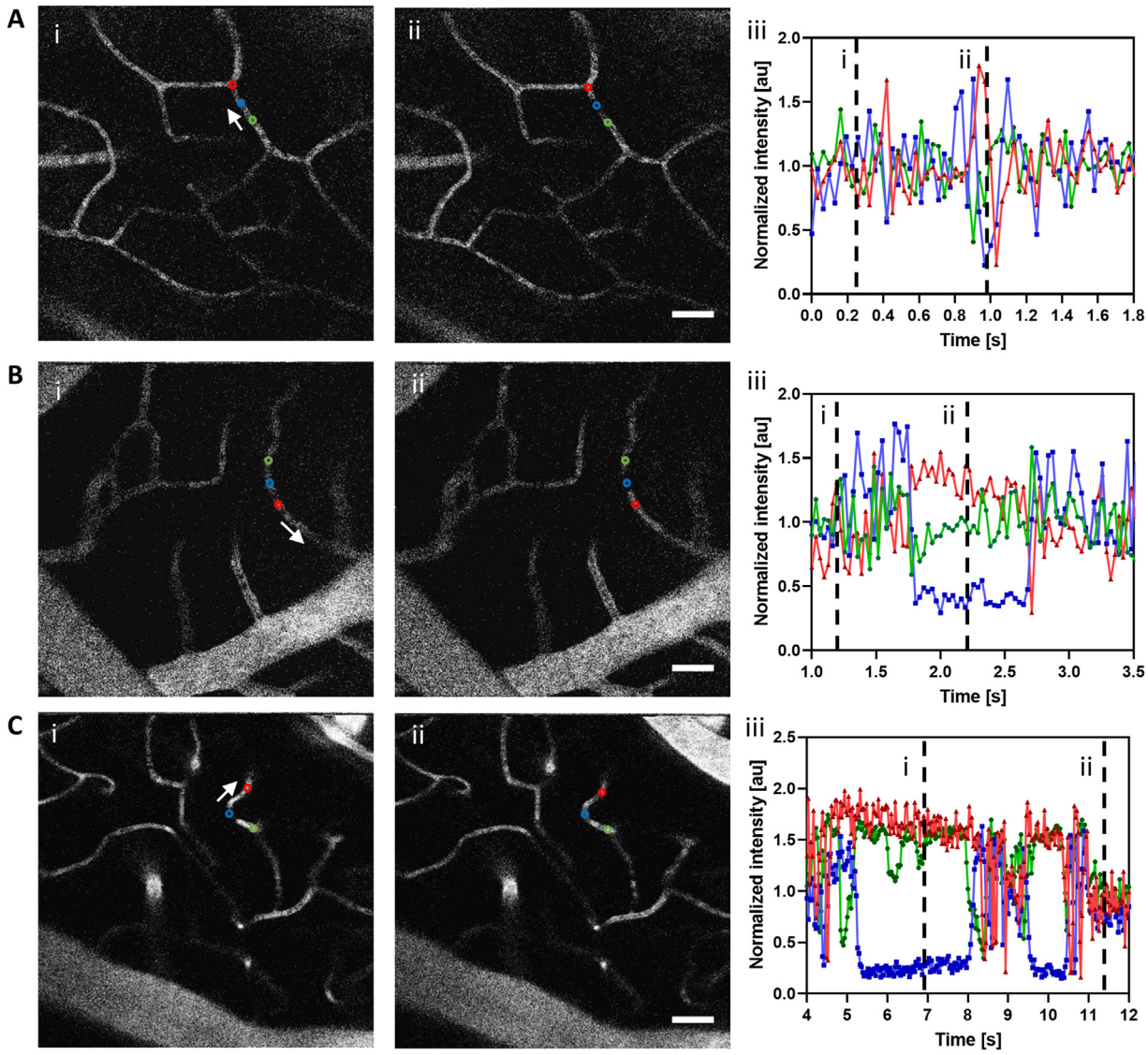

Figure 6. Acoustic Cluster Therapy (ACT®) bubbles temporarily lodging in the vasculature change the intravascular fluorescein isothiocyanate (FITC)–dextran fluorescence intensity. (A–C) Three examples in which one or more ACT® bubbles appeared and temporarily lodged in a blood vessel. Three regions of interest (ROIs) were drawn before (*green*), at (*blue*) and after (*red*) the lodged ACT® bubble in the blood vessel according to the flow direction. The normalized fluorescence intensity for each ROI was plotted showing increase and decrease of the local fluorescence intensity while the ACT® bubbles were lodged. *White arrow* indicates flow direction. Bar = 50 μm.

Immune cell presence in the brain following ACT® treatment

To evaluate the presence of immune cells after ACT® treatment, brain sections from the separate study [29] were stained for F4/80+ cells (macrophages, microglia) and Ly6G+ cells (polymorphonuclear neutrophils) and imaged by confocal local scanning microscopy (CLSM). In tile scans of ACT®-treated and control sections, F4/80+ cells were detected in the perivascular space, parenchymal tissue and cerebral ventricles (Fig. 12A, 12B). The majority of Ly6G+ cells were observed as clusters in intravascular or perivascular spaces, while a few were seen as single cells or fragmented cell structures on the capillary wall (Fig. 12). Semiquantification of sections from two depth levels (2.1 and 2.9 mm from the brain surface) revealed a slight increase but no statistical difference in pixels representing F4/80+ cells in ACT®-treated animals 1 h after treatment compared with control animals (Fig. 12C) (20.5 %, p = ns) and 24 h (33.3%, p = ns). The number of Ly6G+ cells was too low for quantification.

High-magnification images revealed that some F4/80+ cells were in different compartments in the brain such as perivascular spaces of the arteriolar and venular vasculature, as well as arteries and veins (Fig. 13). These cells represent either vessel-associated microglia or perivascular macrophages (Fig. 13A). F4/80+ cells present in the brain parenchymal tissue were morphologically distinct from the perivascular cells (Fig. 13C). Those cells had a ramified morphology and were positively co-stained with the microglial marker (TMEM119), classifying them as brain resident parenchymal microglia. Some double-labeled cells had an amoeboid morphology, indicating that they could be in an activated state. Immunofluorescence verified the histological findings of no infiltration of immune cells after ACT® treatment.

Discussion

Acoustic Cluster Therapy has previously been reported to enhance the permeability of the BBB transiently and locally and to facilitate local accumulation of the macromolecule PEG-CW800 and polymeric micelles in the brain parenchyma in mice [28,29]. The present study investigated the mechanism underlying ACT®-induced accumulation of molecules in

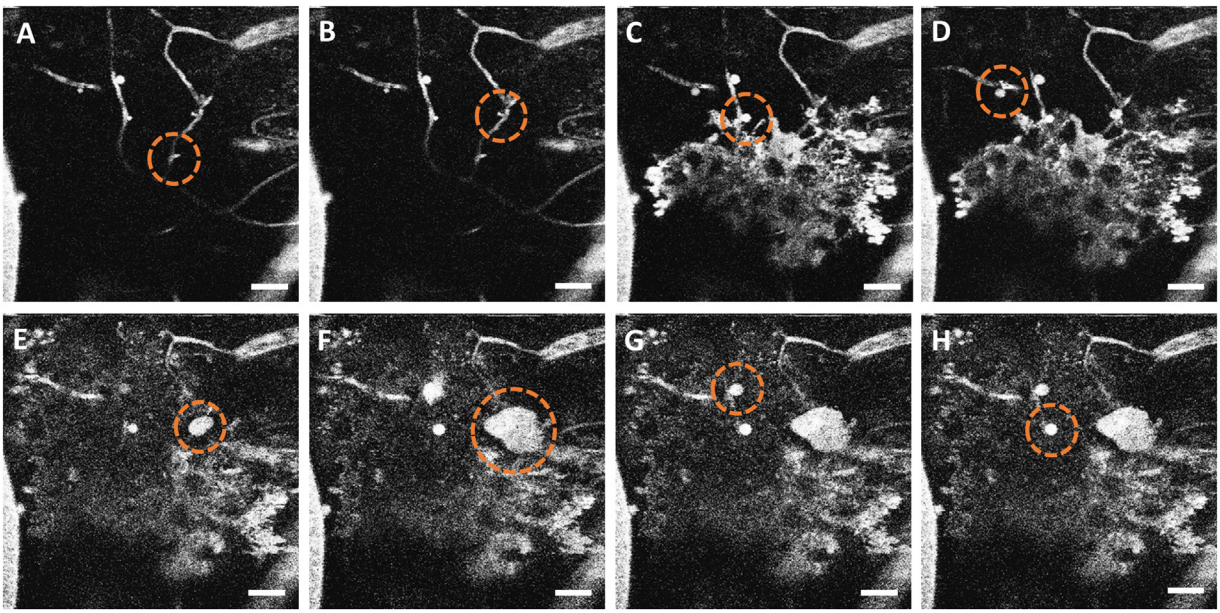

Figure 7. Acoustic Cluster Therapy (ACT®)–induced vessel outpouching and extravasation. Video frames from which the maximum size of each of the outpouchings (A–H) was determined. The video frames originate from videos acquired sequentially. The *dashed circle* indicates the outpouching of interest. Information on the size of the outpouching and corresponding area of extravasation and extravasation time is provided in Table 4. Bar = 50 μm.

Table 4
Diameter of the blood vessel from which the outpouching originated, size of the outpouching, extravasation area, maximum penetration depth of extravasation and duration of extravasation from the outpouching illustrated in Figure 7

Parameter	Outpouching							
	A	B	C	D	E	F	G	H[a]
Diameter blood vessel (μm)	4.4	5.5	5.7	7.2	5.5	5.5	5.7	5.7
Length (μm)	12	10	19	20	44	105	26	24
Width (μm)	7	7	17	18	34	79	22	19
Area (μm^2)	58	43	246	286	1.070	5.950	446	376
Area of extravasation (μm^2)	71.471	170	950	87.527[b]	5.950	9.945	6.107	—
Maximum penetration depth (μm)	200	10	25	183	30	61	61	—
Extravasation duration (s)	~36	~22	~4	~50	~44	~10	~35	—

[a] Outpouching did not leak.
[b] Area of extravasation was hard to determine because of the overlap of the extravasation area with the outpouching area.

the brain using real-time intravital multiphoton microscopy as well as histological analysis *ex vivo*.

It has been suggested that ACT® bubbles have a different working mechanism compared with conventional microbubbles because of their larger size, contact with the endothelium and prolonged residence in the vasculature [20,21]. When exposed to activation ultrasound, microdroplets in ACT® clusters undergo a rapid liquid-to-gas phase shift (ms), forming large ACT® bubbles with a median diameter

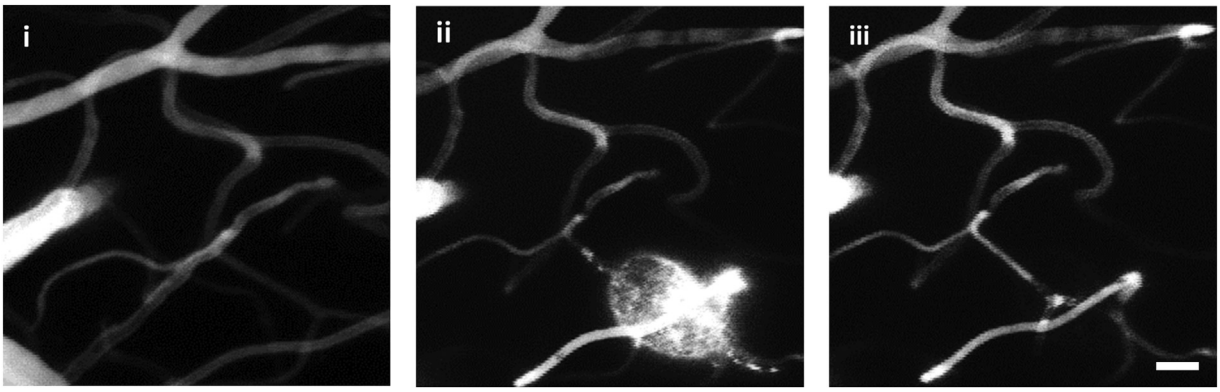

Figure 8. Elliptical fluorescence structure observed on Acoustic Cluster Therapy (ACT®). Maximum projection images of ACT®-induced structure. This might be an activated ACT® bubble or vessel outpouching. (i) In the pre-Z-stack, the elliptical structure was not observed. (ii) In the post-ACT® treatment Z-stack, the elliptical structure appeared, with increased fluorescence intensity in the blood vessel. (iii) By approximately 6 min post-ACT treatment, the elliptical structure had disappeared. Bar = 25 μm.

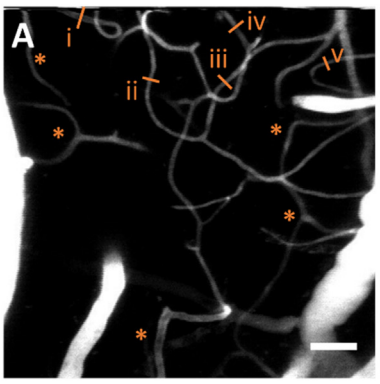

C Diameter blood vessel [µm]

	Pre	Post	Δ
i	7.2	9.5	1.3
ii	5.4	6.9	1.5
iii	5.3	7.4	2.1
iv	6.0	7.7	1.7
v	4.3	5.5	1.2

Figure 9. Maximum projection image of the Z-stack taken (A) before treatment and (B) after treatment. Bar = 50 µm. *Orange lines* mark blood vessels, the diameters of which were measured pre− and post−Acoustic Cluster Therapy (ACT®) treatment. (C) The difference in diameter pre- and post-ACT® treatment. *Blue arrows* mark the leftovers of the outpouching. *Orange asterisks* mark blood vessels that were observed in the pre-XYZ-stack but not in the post-XYZ-stack. The latter is due either to slight misalignment between the pre- and post-XYZ-stacks, movement of the blood vessels with respect to each other, movement of the animal or the vessels' not being functional during the time recording.

of 22 μm (volume of approximately 5600 µm^3) that lodge in the organ-specific microvasculature [20,21,38]. The exact diameter, as well as the time of residence, will depend on the environmental factors affecting ACT® bubbles and varies between *in vitro* and *in vivo* systems in terms of dissolved gas content, system boundaries and flow conditions. Real-time observations of ACT® bubbles in this study revealed that ACT® bubbles in the brain had an average volume of 965 ± 1485 µm^3 (in a 7-µm capillary, the bubble is ~25 µm in length) and reduced lifetime and lodged only for a short time (<1 min).

This is the first time ACT® bubbles have ben imaged in brain capillaries. In previous work, ACT® bubbles were observed to lodge for approximately 5−10 min in rat mesentery [20] and prostate tumors (van Wamel et al. 2016). The shorter residence time observed in the present study may be the result of differences in tissue and vascular properties. Furthermore, in the previous studies, injectable anesthesia was used, whereas gas was used in the present study. The lifetime of ACT® bubbles might be influenced by the nitrogen/oxygen mixture anesthesia carrier gas used, which affected the dissolved gas concentration of the blood and, thereby, the growth and dissolution rate of ACT® bubbles. The choice of anesthesia was dictated by the severity of the surgical procedure. The gas saturation led to suboptimal activation efficacy, affecting ACT® bubble sizes and lifetime and impacting the

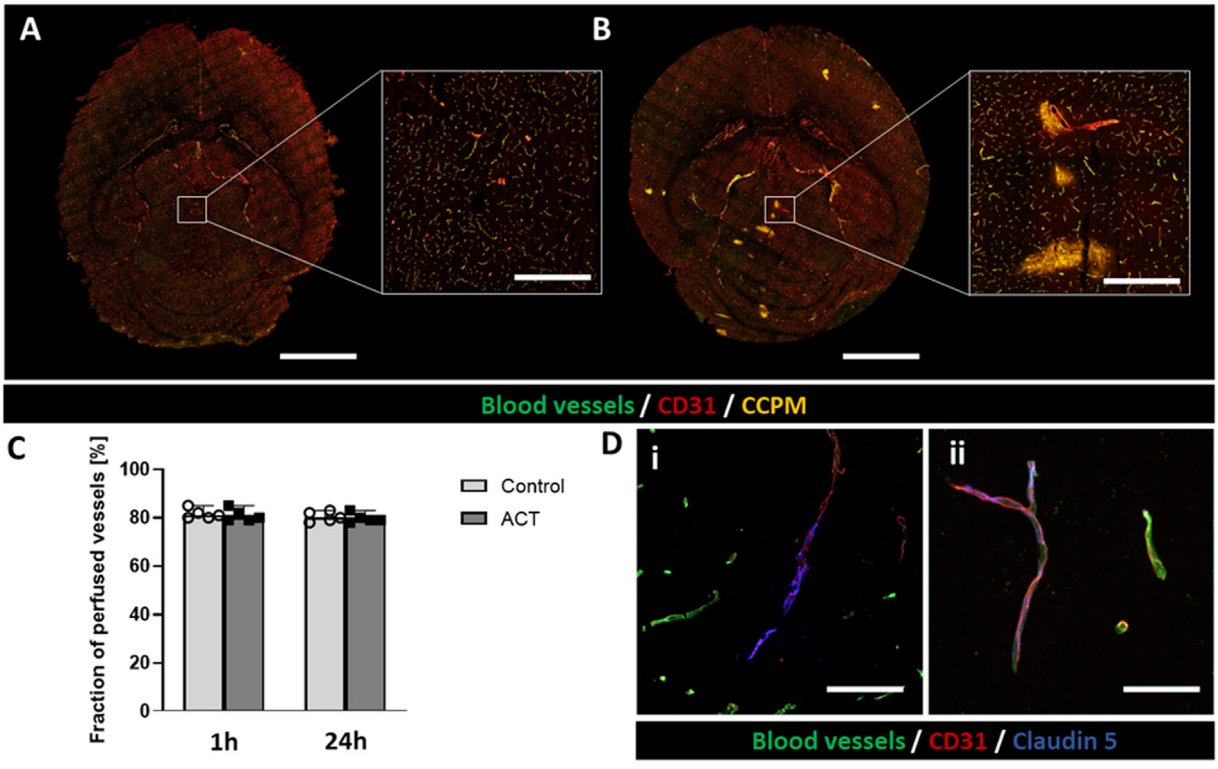

Figure 10. Brain perfusion. Representative immunofluorescence images of brain sections stained for the endothelial marker anti-CD31 (CD31, *red*) and fluorescein isothiocyanate (FITC)−lectin (*green*) to evaluate brain perfusion. (A) One-hour post-treatment control brain. (B) One-hour post−Acoustic Cluster Therapy (ACT®) treatment. (C) The fraction of perfused vessels was calculated by dividing the area fraction of FITC-labeled vessels by the area fraction of CD31 + vessels. Bar = 2 mm and 500 µm. (D) FITC−lectin, anti-CD31 staining and anti-Claudin 5 staining at extravasation sites of polymeric micelles in ACT®-treated animals 1 h post-treatment. Some vessels exhibit a loss of lectin staining but not of CD31 or Claudin 5, indicating vessel occlusion but no irreversible damage. Bar = 50 µm.

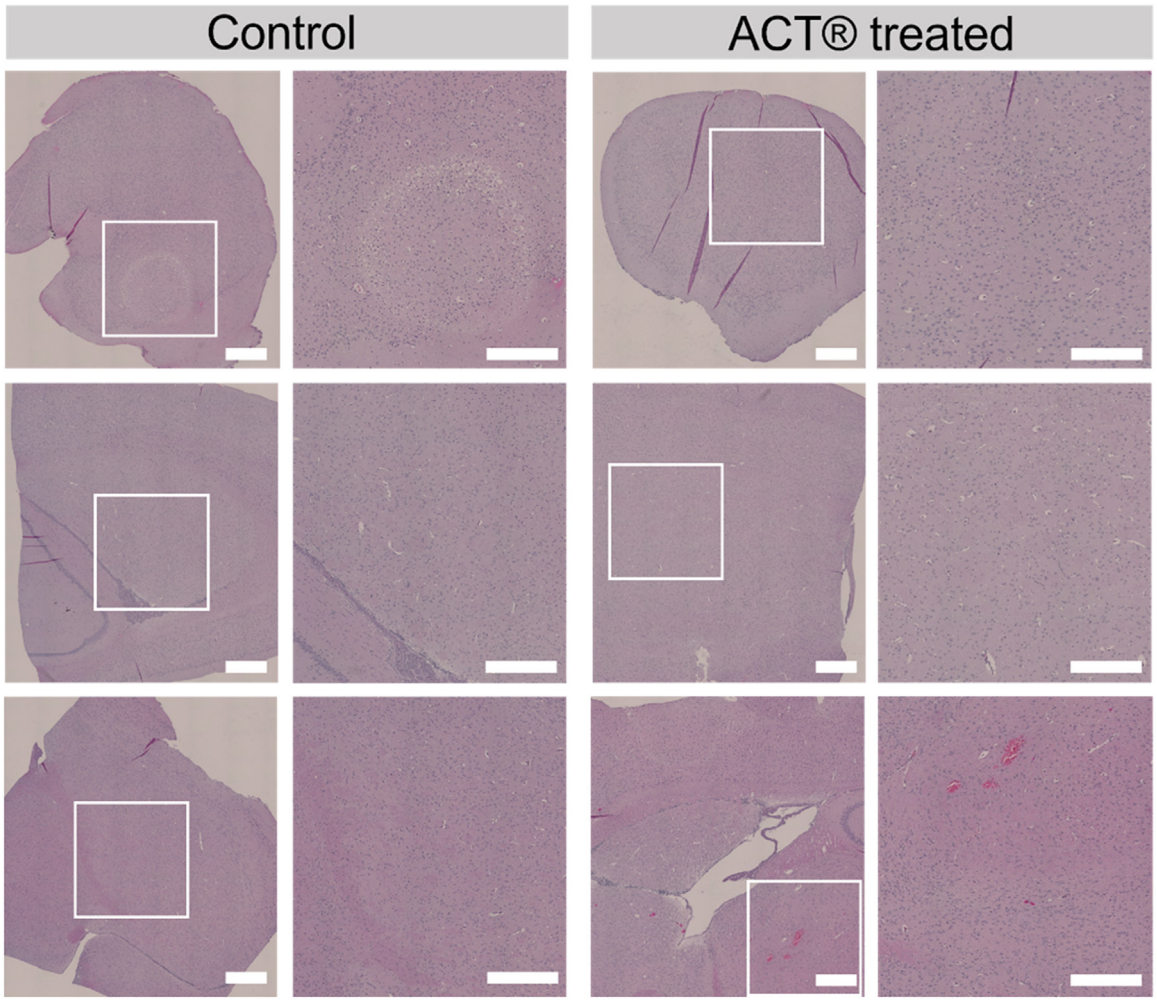

Figure 11. Representative tile scans and high magnification images of regions of interest of HES-stained brain sections of the cranial window containing hemisphere from three different depth levels (0, 1 and 2 mm into the brain). Left: Right hemisphere of a control animal 1 h post-treatment. Right: Right hemisphere of an Acoustic Cluster Therapy–treated animal 1 h post-treatment. Bar = 500 μm.

effectiveness of the activation and enhancement step [39]. The number of ACT® bubbles deposited in the treated area depends on the ultrasound frequency used in the activation step [21,38], and in this study the activation frequency of 0.84 MHz was suboptimal. In addition, the ultrasound pressure at the distance in the cranial window as seen in the ultrasound beam profile was lower compared to previous work (van

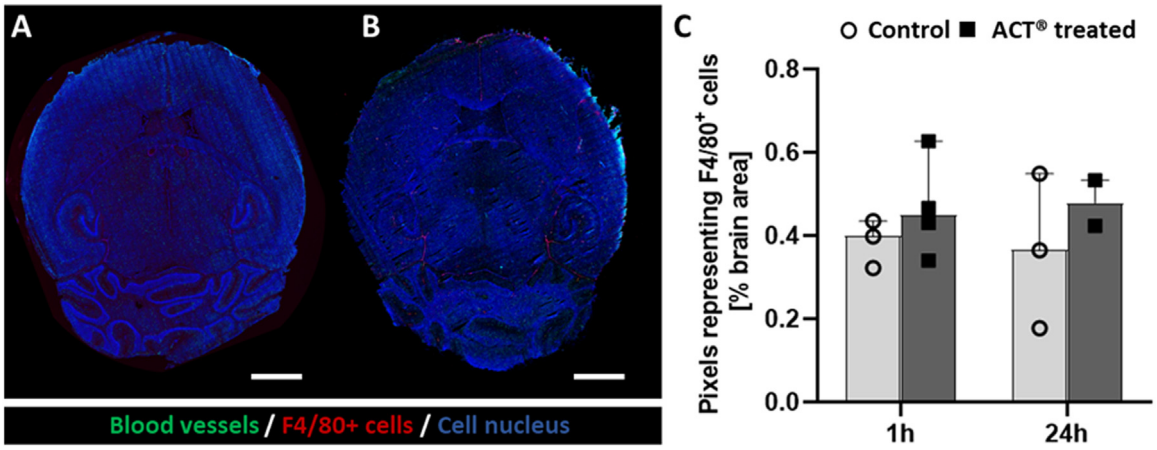

Figure 12. Representative confocal laser scanning microscopy (CLSM) tile scans and percentage of pixels representing F4/80+ immune cells in the brain. (A) Control brain 1 h post-treatment. (B) Acoustic Cluster Therapy–treated brain 1 h post-treatment. F4/80+ cells in *red,* vascular endothelial cells (fluorescein isothiocyanate [FITC]–lectin) in *green* and nuclear DNA (4′,6-diamidino-2-phenylindol [DAPI]) in *blue.* Sections are from a 2.9-mm depth. Bar = 2000 μm. (C) Area percentage of pixels representing F4/80+ cells in 1- and 24-h control and ACT®-treated brains. ACT® versus control (1 h), $p = 0.30$; ACT® versus control (24 h), $p = 0.42$; time points, 1 h versus 24 h, $p = 0.89$.

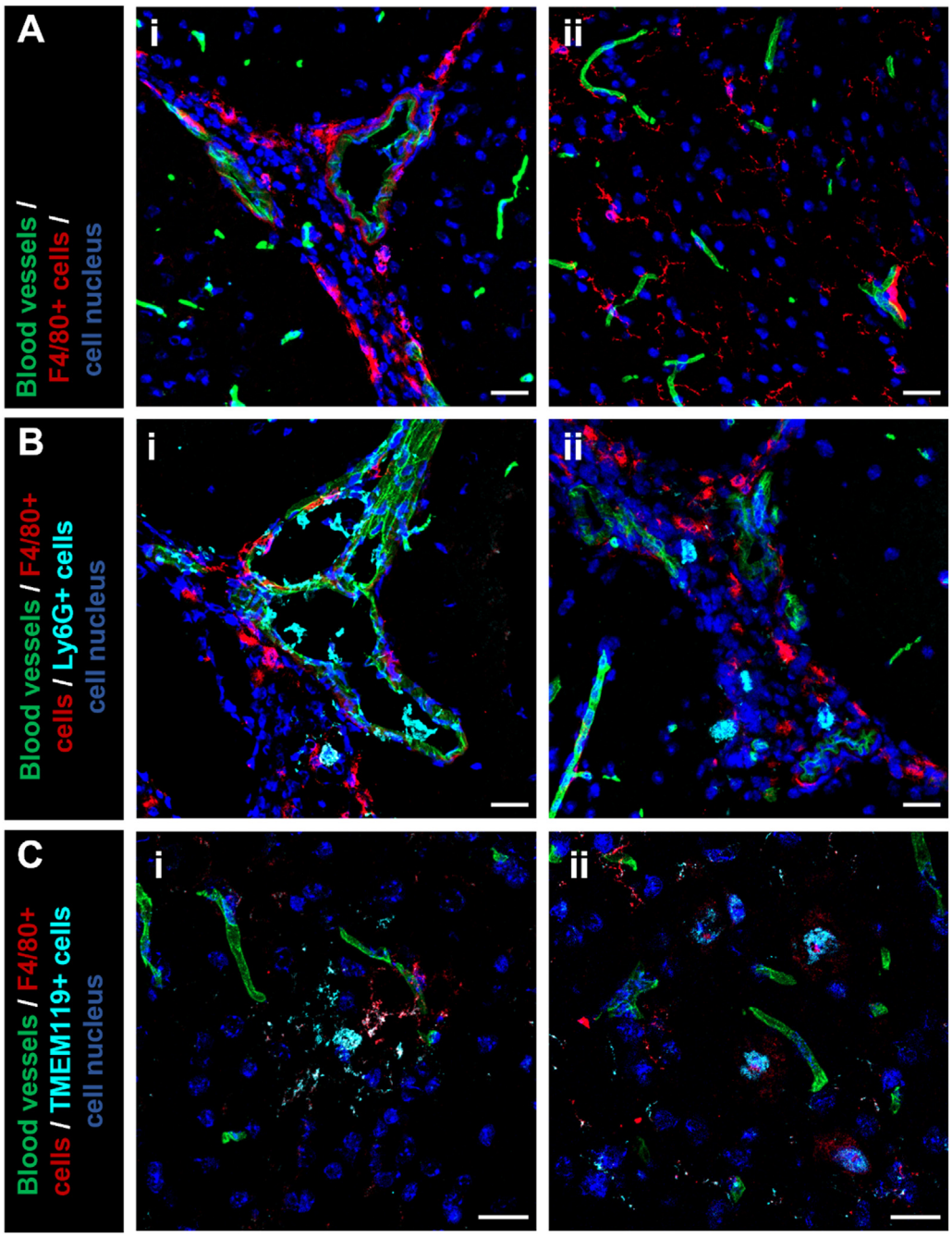

Figure 13. Anatomical location of immune cells in brain tissue 1 h post–Acoustic Cluster Therapy (ACT®) treatment. Brain sections were stained for macrophages (F4/80, *red*) and polymorphonuclear neutrophils (Ly6G, *turquoise*) or microglial marker (TMEM119, *turquoise*), endothelial cell marker (fluorescein isothiocyanate [FITC]–lectin, *green*) and nuclear stain (4′,6-diamidino-2-phenylindol [DAPI], *blue*). (Ai) F4/80+ cells in perivascular spaces of capillaries and larger vessels. (Aii) F4/80+ cells in brain parenchyma. (B) Double-labeled F4/80+/Ly6G+ cells: (i) intravascular; (ii) in perivascular spaces. (C) Microglia: (i) double-labeled F4/80+/TMEM119+ ramified resting microglia; (ii) double-labeled F4/80+/TMEM119+ amoeboid-activated microglia. Bar = 20 μm.

Wamel et al. 2022). The unfavorable frequency used, limited to the available ring transducer, in combination with the relatively low pressure used, probably reduced the activation efficiency significantly. Shorter residence of ACT® bubble in the brain capillaries might also be a result of the structural and physiological organization of the cerebral vasculature rapidly adjusting to various types of stimuli (Erdener et al. 2019). In the brain, arteries give rise to a branching network of arterioles (30–100 μm diameter), pre-capillary arterioles (10–30 μm) and capillaries (<10 μm) that actively regulate blood flow using smooth muscle cells and contractile pericytes. This creates an extensive plasticity that could affect ACT® bubble size and shape and can also affect ACT® bubble efficacy. However, blood gas saturation is probably the primary reason only a small number of ACT® bubbles were observed and lodged inside a vessel in the field of view during imaging.

The ACT® bubbles that were observed to be lodged in the brain vasculature impeded and thereby altered the blood flow, as observed by the increase in FITC–dextran fluorescence intensity upstream of the lodged bubbles. The disturbance of blood flow as well as ACT® bubble activity possibly led to local mechanical effects on the endothelium [40,41]. Mechanical effects could include the development of transmural pressure and microstreaming-induced wall shear stress, which can result in deformation of the vessel wall and possible weakening of the endothelial lining [42,43]. Occlusion of capillaries will also divert blood flow into different segments of the capillary bed, which can induce hemodynamic

changes affecting the direction of wall shear stress [44]. During sonication, vasoconstriction was observed in blood vessels in the field of view. Mechanical stimulation of the endothelium will induce the release of chemical substances such as nitric oxide and prostacyclin, modulating vascular smooth muscle cell and pericyte vasodilatory tone, leading to reversible vasomodulation in the form of vasoconstriction and vasodilation [45,46]. Extension of the vessel diameter can decrease the resistance and increase the blood flow, enhancing perfusion downstream. Reperfusion of occluded vessels can lead to biological effects enhancing extravasation [47,48].

Acoustic Cluster Therapy led to the formation of small saccular outpouchings from the capillaries ranging from 43 to 5950 μm^2. The formation and growth of the outpouchings resembled those of cerebral aneurysms, but because of the smaller size they are referred to as outpouchings [49,50]. Extravasation occurred only from the developed outpouchings and was not observed at other locations. The size of the outpouchings did not correlate with the area of extravasated dextran. Extravasated FITC–dextrans exhibited a heterogeneous pattern, indicating the path of least resistance through the brain`s extracellular matrix. Thus, the penetration depth seemed to depend on the tortuous path and steric hinderance by the extracellular matrix as well as neurons and glial cells, rather than the size of the outpouchings. The duration of extravasation from the outpouchings was between 4 and 50 s, which is rather slow compared with other studies [10,33]. Interesting, the penetration of dextrans into the brain parenchyma stopped while the ultrasound was still on, illustrating that prolonging the ultrasound exposure will not increase the penetration depth.

The observed extravasation pattern is consistent with our earlier study revealing that ACT® facilitated high local accumulation of polymeric micelles in the brain parenchyma [29]. The fluorescent micelles appeared in spots throughout the brain parenchyma, and the area of extravasation and their penetration depth, and the area was similar to the area of the extravasated FITC–dextran found in the present study. The observed extravasation pattern seemed to be ACT® specific. It was not observed before ACT® treatment and, to our knowledge, has not been reported when small contrast agent microbubbles were used. The pattern is different from what was previously observed during real-time intravital imaging of FITC–dextrans and nanoparticles in tumor tissue growing in dorsal window chambers treated with ultrasound and SonoVue [51]. In this case, the distribution of FITC–dextrans was less heterogenous and occurred mainly from vessel branching points. The difference probably reflects the difference between tumor vasculature being chaotic and fenestrated and brain capillaries being dynamic and non-fenestrated and the difference in tumor and brain extracellular matrix [52]. During real-time imaging, extravasation of FITC–dextrans stopped by itself and not when the ultrasound was turned off, indicating that transport across the vessels continues when ACT® bubbles dislodge and flow is re-established. Most affected vessels were still found to be functional with blood flow. Several blood vessels were dilated possibly because of coagulation and subsequent sealing of the endothelium and an increase in blood flow in response to a lack of oxygen. Most dilated vessels still contained RBCs, which could also be observed in excised brains and from T1-Flash MR images [29].

Acoustic Cluster Therapy bubble activity might cause a partial disintegration of the BBB by widening the interendothelial tight junctions supporting paracellular transport across the BBB. At this optical spatial resolution (~400 nm), immunostaining of tight junctions did not reveal any disintegration of tight junctions. However, other studies using immunoelectron microscopy reported that focused ultrasound in conjunction with small contrast agents formed small tight junctional gaps of 15–120 nm [53–57].

Increasing the permeability of the BBB can lead to an acute inflammatory response. However, in HES-stained brain sections, no acute physical damage or fluid formation was seen, and only a small number of resident macrophages, recruited macrophages and infiltrating neutrophils were observed, indicating no inflammatory response. This is in line with previous studies reporting no signs of acute damage to endothelial cells or neurons, microscopic hemorrhage or infiltrating neutrophils in HES-stained brain sections [29]. Immunohistochemistry of sections of entire brains that were treated with ACT® confirmed what was observed with histology. The degree of inflammatory response was assessed quantitatively by immunostaining brain sections for the infiltration of peripheral innate immune cells such as neutrophils and macrophages. No statistically significant difference for vessel-associated or perivascular macrophages and microglia was detected between control and ACT®-treated brain sections. Perivascular macrophages reside in perivascular spaces around blood vessels, while microglia become activated to phagocytose infiltrating components from the blood [58]. A small number of infiltrating neutrophils or fragmented cell structures from neutrophil degradation were detected in perivascular spaces or intravascularly, attached to the vasculature. This might be an indication that ACT® induces a minor immune response in the absence of severe damage. Studies using focused ultrasound in combination with regular microbubbles observed a transient activation of astrocytes and microglia on treatment [59–61]. The degree of the acute immune response after ultrasound is dependent on the duration, microbubble dose and acoustic pressures used [62].

Real-time intravital microscopy is a powerful tool for understanding the mechanism of ACT® bubbles and model drug behavior during ultrasound exposure. To further optimize our experimental setup in new experiments, we would make a dual-frequency ring transducer with optimal frequency for activation of the ACT® bubbles and the subsequent enhancement step. Anesthesia including oxygen should be avoided. These two improvements will allow for more efficient activation of the ACT® bubbles and a possibly longer residence time, making it easier to image more bubbles in the small field of view.

Conclusion

Studying the *in vivo* response of ACT® treatment using real-time imaging of the vasculature in the brain through a cranial window deepened our understanding of the mechanism underlying ACT®, laying the foundation for future experiments towards an efficient ACT® treatment in the clinic. For the future, the mechanism underlying extravasation from ACT®-induced outpouchings, as well as long-term safety effects, should be evaluated further.

Acknowledgments

The authors thank Charissa Poon for the guidance and helpful discussion in terms of the experimental procedure in ring transducer placement as well as Astrid Bjørkøy from the Centre of Advanced Microscopy (CAM) at the faculty of Natural Science for assistance with multiphoton microscopy.

The animals were housed at the Comparative Medicine Core Facility (CoMed, NTNU), and tissue sections were prepared by the Cellular and Molecular Imaging Core Facility (CMIC, NTNU). Illustrations were created with BioRender.com. This work was supported by the Norwegian University of Science and Technology (NTNU, Trondheim, Norway) and the Research Council of Norway under Grant No. Nano2021 262228.

Conflict of interest

E.B.O, S.K., S.H.T., S.S., C.d.L.D. and M.O. declare no competing interests. M.M. is employed by EXACT Therapeutics AS, an ultrasound and microbubble-enhanced therapy company. Employment started after this study was conducted. This work has been used as a patent example.

Data availability statement

The data generated and analyzed during the study are not publicly available but are available from the corresponding author on reasonable request.

Supplementary materials

Supplementary material associated with this article can be found, in the online version, at doi:10.1016/j.ultrasmedbio.2023.01.007.

References

[1] Abbott NJ, Patabendige AA, Dolman DE, Yusof SR, Begley DJ. Structure and function of the blood–brain barrier. Neurobiol Dis 2010;37:13–25.
[2] Pardridge WM. Drug transport across the blood–brain barrier. J Cereb Blood Flow Metab 2012;32:1959–72.
[3] Löscher W, Potschka H. Drug resistance in brain diseases and the role of drug efflux transporters. Nat Rev Neurosci 2005;6:591–602.
[4] Dhuria SV, Hanson LR, Frey II WH. Intranasal delivery to the central nervous system: mechanisms and experimental considerations. J Pharm Sci 2010;99:1654–73.
[5] Lochhead JJ, Thorne RG. Intranasal delivery of biologics to the central nervous system. Adv Drug Del Rev 2012;64:614–28.
[6] Rapoport SI. Osmotic opening of the blood–brain barrier: principles, mechanism, and therapeutic applications. Cell Mol Neurobiol 2000;20:217–30.
[7] White E, Woolley M, Bienemann A, Johnson DE, Wyatt M, Murray G, et al. A robust MRI-compatible system to facilitate highly accurate stereotactic administration of therapeutic agents to targets within the brain of a large animal model. J Neurosci Methods 2011;195:78–87.
[8] Hynynen K, McDannold N, Vykhodtseva N, Jolesz FA. Noninvasive MR imaging-guided focal opening of the blood–brain barrier in rabbits. Radiology 2001;220:640–6.
[9] Liu HL, Fan CH, Ting CY, Yeh CK. Combining microbubbles and ultrasound for drug delivery to brain tumors: current progress and overview. Theranostics 2014;4:432–44.
[10] Nhan T, Burgess A, Cho EE, Stefanovic B, Lilge L, Hynynen K. Drug delivery to the brain by focused ultrasound induced blood–brain barrier disruption: quantitative evaluation of enhanced permeability of cerebral vasculature using two-photon microscopy. J Control Release 2013;172:274–80.
[11] Olsman M, Sereti V, Mühlenpfordt M, Johnsen KB, Andresen TL, Urquhart AJ, et al. Focused ultrasound and microbubble treatment increases delivery of transferrin receptor-targeting liposomes to the brain. Ultrasound Med Biol 2021;47:1343–55.
[12] Poon C, McMahon D, Hynynen K. Noninvasive and targeted delivery of therapeutics to the brain using focused ultrasound. Neuropharmacology 2017;120:20–37.
[13] Wei KC, Chu PC, Wang HYJ, Huang CY, Chen PY, Tsai HC, et al. Focused ultrasound-induced blood–brain barrier opening to enhance temozolomide delivery for glioblastoma treatment: a preclinical study. PLoS One 2013;8:e58995.
[14] Tung YS, Vlachos F, Feshitan JA, Borden MA, Konofagou EE. The mechanism of interaction between focused ultrasound and microbubbles in blood–brain barrier opening in mice. J Acoust Soc Am 2011;130:3059–67.
[15] Carpentier A, Canney M, Vignot A, Reina V, Beccaria K, Horodyckid C, et al. Clinical trial of blood–brain barrier disruption by pulsed ultrasound. Sci Transl Med 2016;8:343re2.
[16] Mainprize T, Lipsman N, Huang Y, Meng Y, Bethune A, Ironside S, et al. Blood–brain barrier opening in primary brain tumors with non-invasive MR-guided focused ultrasound: a clinical safety and feasibility study. Sci Rep 2019;9:1–7.
[17] Meng Y, Hynynen K, Lipsman N. Applications of focused ultrasound in the brain: from thermoablation to drug delivery. Nat Rev Neurol 2020;17:7–22.
[18] Kooiman K, Vos HJ, Versluis M, de Jong N. Acoustic behavior of microbubbles and implications for drug delivery. Adv Drug Del Rev 2014;72:28–48.
[19] Delalande A, Kotopoulis S, Postema M, Midoux P, Pichon C. Sonoporation: mechanistic insights and ongoing challenges for gene transfer. Gene 2013;525:191–9.
[20] Sontum P, Kvale S, Healey AJ, Skurtveit R, Watanabe R, Matsumura M, et al. Acoustic Cluster Therapy (ACT)—A novel concept for ultrasound mediated, targeted drug delivery. Int J Pharm 2015;495:1019–27.
[21] Healey AJ, Sontum PC, Kvale S, Eriksen M, Bendiksen R, Tornes A, et al. Acoustic cluster therapy: in vitro and ex vivo measurement of activated bubble size distribution and temporal dynamics. Ultrasound Med Biol 2016;42:1145–66.
[22] van Wamel A, Healey A, Sontum PC, Kvale S, Bush N, Bamber J, et al. Acoustic Cluster Therapy (ACT)—pre-clinical proof of principle for local drug delivery and enhanced uptake. J Control Release 2016;224:158–64.
[23] Myhre O, Bjørgan M, Grant D, Hustvedt SO, Sontum PC, Dirven H. Safety assessment in rats and dogs of Acoustic Cluster Therapy, a novel concept for ultrasound mediated, targeted drug delivery. Pharmacol Res Perspect 2016;4:e00274.
[24] Bush N, Healey A, Shah A, Box G, Kirkin V, Eccles S, et al. Theranostic attributes of Acoustic Cluster Therapy and its use for enhancing the effectiveness of liposomal doxorubicin treatment of human triple negative breast cancer in mice. Front Pharmacol 2020;11:75.
[25] Bush NL, Healey A, Shah A, Box G, Kirkin V, Kotopoulis S, et al. Therapeutic dose response of acoustic cluster therapy in combination with irinotecan for the treatment of human colon cancer in mice. Front Pharmacol 2019;10:1299.
[26] Kotopoulis S, Stigen E, Popa M, Safont MM, Healey A, Kvale S, et al. Sonoporation with Acoustic Cluster Therapy (ACT®) induces transient tumour volume reduction in a subcutaneous xenograft model of pancreatic ductal adenocarcinoma. J Control Release 2017;245:70–80.
[27] van Wamel A, Sontum PC, Healey A, Kvale S, Bush N, Bamber J, et al. Acoustic Cluster Therapy (ACT) enhances the therapeutic efficacy of paclitaxel and Abraxane® for treatment of human prostate adenocarcinoma in mice. J Control Release 2016;236:15–21.
[28] Åslund AK, Snipstad S, Healey A, Kvale S, Torp SH, Sontum PC, et al. Efficient enhancement of blood–brain barrier permeability using Acoustic Cluster Therapy (ACT). Theranostics 2017;7:23–30.
[29] Olsman M, Mühlenpfordt M, Olsen EB, Torp SH, Kotopoulis S, Rijcken CJ, et al. Acoustic Cluster Therapy (ACT®) enhances accumulation of polymeric micelles in the murine brain. J Control Release 2021;337:285–95.
[30] Caskey CF, Stieger SM, Qin S, Dayton PA, Ferrara KW. Direct observations of ultrasound microbubble contrast agent interaction with the microvessel wall. J Acoust Soc Am 2007;122:1191–200.
[31] Helfield B, Chen X, Watkins SC, Villanueva FS. Biophysical insight into mechanisms of sonoporation. Proc Natl Acad Sci USA 2016;113:9983–8.
[32] Raymond SB, Skoch J, Hynynen K, Bacskai BJ. Multiphoton imaging of ultrasound/Optison mediated cerebrovascular effects in vivo. J Cereb Blood Flow Metab 2007;27:393–403.
[33] Cho EE, Drazic J, Ganguly M, Stefanovic B, Hynynen K. Two-photon fluorescence microscopy study of cerebrovascular dynamics in ultrasound-induced blood–brain barrier opening. J Cereb Blood Flow Metab 2011;31:1852–62.
[34] Poon C, Mühlenpfordt M, Olsman M, Kotopoulis S, de Lange Davies C, et al. Real-time intravital multiphoton microscopy to visualize focused ultrasound and microbubble treatments to increase blood–brain barrier permeability. J Vis Exp 2022;180:e62235.
[35] Burgess A, Cho EE, Shaffaf L, Nhan T, Poon C, Hynynen K. The use of two-photon microscopy to study the biological effects of focused ultrasound on the brain In: Konig K, editor. Multiphoton Microscopy in the Biomedical Sciences XII SPIE Proc 2012;8226:466–72.
[36] Yddal T, Gilja O H, Cochran S, Postema M, Kotopoulis S. Glass-windowed ultrasound transducers. Ultrasonics 2016;68:108–19.
[37] Andersen KK, Healey A, Bush NL, Frijlink ME, Hoff L. A harmonic dual-frequency transducer for acoustic cluster therapy. Ultrasound Med Biol 2019;45:2381–90.
[38] van Wamel A, Mühlenpfordt M, Hansen R, Healey A, Villanueva FS, Kotopoulis S, et al. Ultrafast microscopy imaging of acoustic cluster therapy bubbles: activation and oscillation. Ultrasound Med Biol 2022;48:1840–57.
[39] Mullin L, Gessner R, Kwan J, Kaya M, Borden MA, Dayton PA. Effect of anesthesia carrier gas on in vivo circulation times of ultrasound microbubble contrast agents in rats. Contrast Media Mol Imaging 2011;6:126–31.
[40] Hosseinkhah N. An ultrasound contrast agent microbubble in a microvessel: a numerical approach. University of Toronto; 2015.
[41] Chiu JJ, Chien S. Effects of disturbed flow on vascular endothelium: pathophysiological basis and clinical perspectives. Physiol Rev 2011;91:327–87.
[42] Chen H, Kreider W, Brayman AA, Bailey MR, Matula TJ. Blood vessel deformations on microsecond time scales by ultrasonic cavitation. Phys Rev Lett 2011;106:034301.
[43] Chen H, Brayman AA, Evan AP, Matula TJ. Preliminary observations on the spatial correlation between short-burst microbubble oscillations and vascular bioeffects. Ultrasound Med Biol 2012;38:2151–62.
[44] Itoh Y, Suzuki N. Control of brain capillary blood flow. J Cereb Blood Flow Metab 2012;32:1167–76.
[45] McCarron R, Chen Y, Tomori T, Strasser A, Mechoulam R, Shohami E, et al. Endothelial-mediated regulation of cerebral microcirculation. J Physiol Pharmacol 2006;57:133–44.
[46] Maruo A, Hamner CE, Rodrigues AJ, Higami T, Greenleaf JF, Schaff HV. Nitric oxide and prostacyclin in ultrasonic vasodilatation of the canine internal mammary artery. Ann Thorac Surg 2004;77:126–32.
[47] Gourdin MJ, Bree B, De Kock M. The impact of ischaemia–reperfusion on the blood vessel. Eur J Anaesthesiol 2009;26:537–47.
[48] Arvanitis CD, Gyongy M, Bazan-Peregrino M, Rifai B, Seymour LW, Coussios CC. Passive mapping of cavitation activity for monitoring of drug delivery. J Acoust Soc Am 2010;127:1977.
[49] Erdener ŞE, Tang J, Sajjadi A, Kılıç K, Kura S, Schaffer CB, et al. Spatio-temporal dynamics of cerebral capillary segments with stalling red blood cells. J Cereb Blood Flow Metab 2019;39:886–900.
[50] Sadasivan C, Fiorella DJ, Woo HH, Lieber BB. Physical factors effecting cerebral aneurysm pathophysiology. Ann Biomed Eng 2013;41:1347–65.
[51] Yemane PT, Aslund AKO, Snipstad S, Bjorkoy A, Grendstad K, Berg S, et al. Effect of ultrasound on the vasculature and extravasation of nanoscale particles imaged in real time. Ultrasound Med Biol 2019;45:3028–41.
[52] Guyon J, Chapouly C, Andrique L, Bikfalvi A, Daubon T. The normal and brain tumor vasculature: morphological and functional characteristics and therapeutic targeting. Front Physiol 2021;12:622615.
[53] Sheikov N, McDannold N, Sharma S, Hynynen K. Effect of focused ultrasound applied with an ultrasound contrast agent on the tight junctional integrity of the brain microvascular endothelium. Ultrasound Med Biol 2008;34:1093–104.
[54] Ohta S, Kikuchi E, Ishijima A, Azuma T, Sakuma I, Ito T. Investigating the optimum size of nanoparticles for their delivery into the brain assisted by focused ultrasound-induced blood–brain barrier opening. Sci Rep 2020;10:1–13.

[55] Shen Y, Guo J, Chen G, Chin CT, Chen X, et al. Delivery of liposomes with different sizes to mice brain after sonication by focused ultrasound in the presence of microbubbles. Ultrasound Med Biol 2016;42:1499–511.
[56] Chen H, Konofagou EE. The size of blood–brain barrier opening induced by focused ultrasound is dictated by the acoustic pressure. J Cereb Blood Flow Metab 2014;34:1197–204.
[57] Marty B, Larrat B, Van Landeghem M, Robic C, Robert P, Port M, et al. Dynamic study of blood–brain barrier closure after its disruption using ultrasound: a quantitative analysis. J Cereb Blood Flow Metab 2012;32:1948–58.
[58] Koizumi T, Kerkhofs D, Mizuno T, Steinbusch HW, Foulquier S. Vessel-associated immune cells in cerebrovascular diseases: from perivascular macrophages to vessel-associated microglia. Front Neurosci 2019;13:1291.
[59] Kovacs ZI, Kim S, Jikaria N, Qureshi F, Milo B, Lewis BK, et al. Disrupting the blood–brain barrier by focused ultrasound induces sterile inflammation. Proc Natl Acad Sci USA 2017;114:E75–84.
[60] Poon C, Pellow C, Hynynen K. Neutrophil recruitment and leukocyte response following focused ultrasound and microbubble mediated blood–brain barrier treatments. Theranostics 2021;11:1655.
[61] Silburt J, Lipsman N, Aubert I. Disrupting the blood–brain barrier with focused ultrasound: Perspectives on inflammation and regeneration. Proc Natl Acad Sci USA 2017;114:E6735–6.
[62] McMahon D, Hynynen K. Acute inflammatory response following increased blood–brain barrier permeability induced by focused ultrasound is dependent on microbubble dose. Theranostics 2017;7:3989.